

Journal of Materials Chemistry A

Materials for energy and sustainability

Accepted Manuscript

This article can be cited before page numbers have been issued, to do this please use: Q. Pang, H. Zhao, R. Lian, Q. Fu, Y. Wei, A. Sarapulova, J. Sun, C. Wang, G. Chen and H. Ehrenberg, *J. Mater. Chem. A*, 2020, DOI: 10.1039/D0TA00858C.



This is an Accepted Manuscript, which has been through the Royal Society of Chemistry peer review process and has been accepted for publication.

Accepted Manuscripts are published online shortly after acceptance, before technical editing, formatting and proof reading. Using this free service, authors can make their results available to the community, in citable form, before we publish the edited article. We will replace this Accepted Manuscript with the edited and formatted Advance Article as soon as it is available.

You can find more information about Accepted Manuscripts in the [Information for Authors](#).

Please note that technical editing may introduce minor changes to the text and/or graphics, which may alter content. The journal's standard [Terms & Conditions](#) and the [Ethical guidelines](#) still apply. In no event shall the Royal Society of Chemistry be held responsible for any errors or omissions in this Accepted Manuscript or any consequences arising from the use of any information it contains.

View Article Online
DOI: 10.1039/C9TA00858C

Understanding the Mechanism of Byproduct Formation with *In Operando* Synchrotron Techniques and Its Effects on the Electrochemical Performance of VO₂(B) Nanoflakes in Aqueous Rechargeable Zinc Batteries

Qiang Pang^{a,c,d,#}, Hainan Zhao^{a,#}, Ruqian Lian^a, Qiang Fu^{b,*}, Yingjin Wei^{a,*}, Angelina Sarapulova^b, Junqi Sun^d, Chunzhong Wang^a, Gang Chen^a, Helmut Ehrenberg^b

^a Key Laboratory of Physics and Technology for Advanced Batteries (Ministry of Education), College of Physics, Jilin University, Qianjin Street 2699, Changchun 130012, P. R. China.

^b Institute for Applied Materials (IAM), Karlsruhe Institute of Technology (KIT), Hermann-von-Helmholtz-Platz 1, D-76344 Eggenstein-Leopoldshafen, Germany.

^c School of Science, Dalian Maritime University, Linghai Road 1, Dalian 116026, P. R. China.

^d State Key Laboratory of Supramolecular Structure and Materials, College of Chemistry, Jilin University, Qianjin Street 2699, Changchun 130012, P. R. China.

Corresponding authors: yjwei@jlu.edu.cn (Y.J. Wei); qiang.fu@kit.edu (Q. Fu)

#: These authors contributed equally to this work

Abstract

View Article Online
DOI: 10.1039/D0TA00858C

The monoclinic VO₂(B) nanoflakes prepared by hydrothermal method displayed superior electrochemical performances in 1 M ZnSO₄ electrolyte. The reaction mechanisms of VO₂(B) and the essential causes of byproduct formation in aqueous rechargeable zinc batteries (ARZBs) were comprehensively studied by electrochemical measurements in combining with *in operando* synchrotron techniques and first-principles calculations. During electrochemical processes, the electrode underwent a reversible solid-solution reaction between VO₂(B) and Zn_{0.44}VO₂ with simultaneous formation/decomposition of (Zn(OH)₂)₃(ZnSO₄)·5H₂O byproduct. Importantly, the formation of byproduct was attributed to [Zn(H₂O)₆]²⁺ dehydration, where the byproduct could protect the electrode material from corrosion of H₃O⁺ and facilitate the dehydration process of Zn²⁺ on the electrode-electrolyte interface. The byproducts could facilitate the migration of Zn²⁺ on the electrode surface due to their three-dimensional pathways. In addition, the electrochemical performance of VO₂(B) and the byproduct in ZnSO₄ electrolyte were compared with those in Zn(CF₃SO₃)₂ and Zn(NO₃)₂. An appropriate electrolyte (1 M Zn(CF₃SO₃)₂) to form a byproduct with largely expanded ionic pathways was proven to further improve the electrochemical performance of VO₂(B). This work not only provides a deep understanding of the Zn²⁺ storage mechanism in VO₂(B) but also establishes a clear relationship between the byproducts and electrochemical performances of vanadium-based electrode materials in ARZBs.

Keywords: Aqueous Rechargeable Zinc Batteries; Byproduct; *In Operando* Synchrotron Techniques; Electrochemical Performance; VO₂;

1. Introduction

The continuous development of renewable energy resources is calling for more competitive and sustainable energy storage technologies to better match the electric supply with demand in smart grids. But, conventional lithium-ion batteries (LIBs) are not the first choice mainly due to their high cost and safety concerns. In view of this, aqueous rechargeable zinc batteries (ARZBs) have received tremendous attention owing to¹⁻³: 1) the high safety of aqueous electrolytes; 2) the easy manufacturing without strict control of moisture and oxygen; 3) the sufficient abundance, low cost, high theoretical capacity (820 mA h g⁻¹; 5851 mA h cm⁻³), low potential (-0.76 V vs. standard hydrogen electrode) of zinc metal, which can be directly used as the negative electrode. A major reason that hinders the practical applications of ARZBs is the lack of high-performance positive electrode materials that can allow reversible Zn²⁺ storage. Although the radius of Zn²⁺ (0.74 Å) is very similar to that of Li⁺ (0.76 Å), the larger mass and double valance of Zn²⁺ bring about low solid-state mobility in the electrode bulk and poor interfacial charge transfer efficiency due to the strong solvation of Zn²⁺ and ion-pairs formation in water^{4,5}.

Many efforts have been made on exploration of high-performance positive electrode materials for ARZBs including Prussian blue analogs (such as zinc hexacyanoferrate ZnHCF and copper hexacyanoferrate CuHCF)⁶⁻⁸, Mn-based oxides (such as MnO₂, Mn₂O₃, and Mn₃O₄)⁹⁻¹⁷, and V-based oxides (such as Zn_{0.25}V₂O₅·nH₂O, V₂O₅, Ca_{0.25}V₂O₅·nH₂O, Na_{0.33}V₂O₅, V₂O₅·nH₂O, LiV₃O₈, and V_{1-x}Al_xO_{1.52}(OH)_{0.77})¹⁸⁻²⁷. In these materials, the open framework or layered structure of Mn- and V-based oxides are prone to collapse after prolonged cycles giving rise to poor cycling stability^{3, 28}. Researchers have made great efforts to solve these issues. For instance, Liu *et al.*¹⁰ demonstrated that α-MnO₂ underwent a conversion reaction from the α-phase to a layered structure in ARZBs and its cyclic stability was greatly improved by adding a certain amount of MnSO₄ in the electrolyte to suppress Mn²⁺ dissolution. Nazar *et al.*²¹ showed that Zn²⁺ pre-intercalated V₂O₅ (Zn_{0.25}V₂O₅·nH₂O) delivered a high specific capacity of 300 mA h g⁻¹ with excellent rate capability. Mai *et al.*²⁵ reported that the structural water of V₂O₅·nH₂O could work as a charge screening media during redox reactions, which increased the interlayer distance of the material and decreased the effective charge of Zn²⁺ by solvation. In addition to these great success, it has been

frequently reported that a mass of complex byproducts were produced/decomposed during the discharge/charge cycling of vanadium oxides such as $\text{VO}_{1.52}(\text{OH})_{0.77}$ ²⁷, $\text{Zn}_2\text{V}_2\text{O}_7$ ²⁹, $\text{Na}_2\text{V}_6\text{O}_{16}\cdot 3\text{H}_2\text{O}$ ³⁰, $\text{NaV}_3\text{O}_8\cdot 1.5\text{H}_2\text{O}$ ³¹, and $\text{NH}_4\text{V}_4\text{O}_{10}$ ³². However, the underlying causes of byproduct formation and decomposition are still unclear and the effect of byproducts on the electrochemical performance of ARZBs has been rarely investigated.

Among all kinds of vanadium oxides, monoclinic $\text{VO}_2(\text{B})$ has been studied as a promising electrode material for aqueous and non-aqueous rechargeable batteries. $\text{VO}_2(\text{B})$ is built up by corner- and edge-sharing VO_6 octahedral that ensure good structural integrity against insertion of guest cations including alkali cations (Li^+ , Na^+) and multivalent cations (Zn^{2+} , Mg^{2+})³³⁻³⁵. Moreover, the large tunnel (0.82 nm^2) between connected V_4O_{10} layers is beneficial for rapid insertion/de-insertion of guest cations. For example, when $\text{VO}_2(\text{B})$ nanofibers were used in ARZBs³⁶, it exhibited a high reversible capacity of 357 mA h g^{-1} and excellent rate capability with a specific capacity of 171 mA h g^{-1} at 300 C rate. In spite of the excellent electrochemical performance in ARZBs, the structure changes of $\text{VO}_2(\text{B})$ during electrochemical processes is still in debate. There are at least three different viewpoints with respect to the structure changes of $\text{VO}_2(\text{B})$ in ARZBs. Myung *et al.*³⁷ reported that $\text{VO}_2(\text{B})$ underwent a solid solution reaction during Zn^{2+} insertion. While, Wang *et al.*³⁸ showed that $\text{VO}_2(\text{B})$ underwent an irreversible phase transition from $\text{VO}_2(\text{B})$ to bilayered $\text{V}_2\text{O}_5\cdot n\text{H}_2\text{O}$ during initial Zn^{2+} uptake/removal. Niu *et al.*³⁴ reported that $\text{VO}_2(\text{B})$ went through a reversible phase transformation from monoclinic $\text{VO}_2(\text{B})$ to tetragonal $\text{VO}_2(\text{R})$. To better understand the electrochemical mechanism of $\text{VO}_2(\text{B})$ in ARZBs especially the structure properties during charge-discharge cycling, *in operando* synchrotron characterizations in combination with comprehensive electrochemical analysis are strongly suggested to study the composition and structure changes of the electrode during Zn^{2+} insertion/de-insertion. The extremely bright, high flux and high-energy synchrotron radiation provides many advantages such as deep penetration into the sample, high-quality data, and real-time diffraction. In particular, *in operando* synchrotron study can effectively avoid the unpredictable contamination and irreversible changes of highly reactive samples during material

preparation, handling, and transportation, which can provide more reliable and precise data for analysis.

Based on the above consideration, herein, we used monoclinic $\text{VO}_2(\text{B})$ as an example material to study the mechanism of byproduct formation/decomposition and its effects on the electrochemical performance of V-based ARZBs. $\text{VO}_2(\text{B})$ nanoflakes were prepared by a simple hydrothermal method. The detailed structure evolution and reaction mechanism of $\text{VO}_2(\text{B})$ in ARZBs were carefully studied *via in operando* synchrotron diffraction and X-ray absorption spectroscopy. The mechanism of byproduct formation and decomposition in different aqueous electrolytes was analyzed. Moreover, the effects of byproducts on facilitating the dehydration process of Zn^{2+} and improving the charge transfer kinetics of the electrode were revealed by electrochemical measurements. The results may help researchers to understand the Zn^{2+} storage properties in $\text{VO}_2(\text{B})$ and the importance of interfacial reactions between the electrolyte and electrode in ARZBs.

2. Results and Discussion

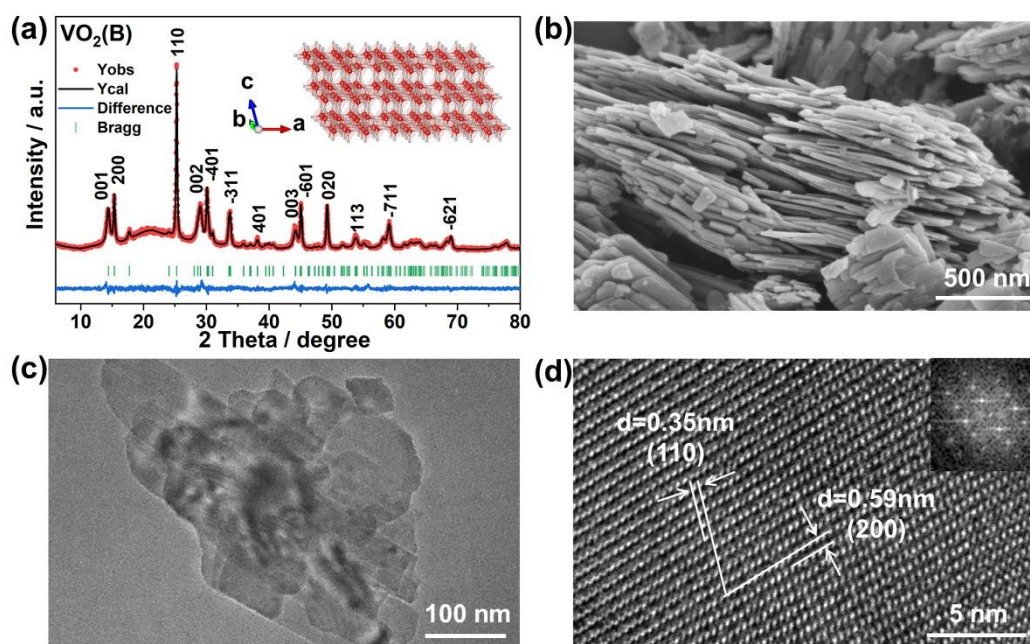


Figure 1. Structure and morphology characterizations of the as-prepared $\text{VO}_2(\text{B})$ sample: (a) Rietveld refinement from X-ray diffraction data of $\text{VO}_2(\text{B})$ nanoflakes and crystal structure (inset) (Cu K_α wavelength $\lambda=1.54184 \text{ \AA}$), (b) SEM image, (c) TEM

image, and (d) HR-TEM image and fast Fourier-transform pattern (inset) of the VO₂(B) nanoflakes.

2.1 Material characterizations. The crystal structure of the as-synthesized VO₂(B) was confirmed by powder X-ray diffraction (XRD). All the characteristic reflections can be indexed to monoclinic VO₂(B) (space group *C2/m*, see Rietveld refinement result in **Figure 1a**) without any impurity phases. The lattice parameters of the material were determined as $a = 12.065 \text{ \AA}$, $b = 3.699 \text{ \AA}$, $c = 6.427 \text{ \AA}$, $\beta = 107.013^\circ$, in good agreement with previous work^{39, 40}. Rietveld refinement showed that the volume weighted average crystallite size perpendicular to the *c*-axis is about 10-times larger than along the *c*-axis. Inset of **Figure 1a** shows the schematic structure of VO₂(B), which confirmed a large tunnel size of 0.82 nm² between connected V₄O₁₀ layers. The morphology and microstructure of VO₂(B) were observed by scanning electron microscopy (SEM). The material was composed of micrometer-sized particles assembled by nanoflakes with thickness of ~ 50 nm (**Figure 1b**). Transmission electron microscopy (TEM) further revealed that the nanoflakes were several hundred nanometers in width and length (**Figure 1c**), in good agreement with Rietveld refinement result. In addition, TEM also showed the almost transparent feature of VO₂(B), indicating a very thin nanoflake structure of the material. The different contrast zones in the TEM image may be attributed to non-uniform thickness distribution of the nanoflakes. A high-resolution TEM image of the VO₂(B) nanoflakes showed a set of clear lattice fringes (**Figure 1d**), which were in good agreement with the spacing distances of (110) ($d = 0.35 \text{ nm}$) and (200) planes ($d = 0.59 \text{ nm}$). The fast Fourier-transform pattern (inset of **Figure 1d**) further verified the single-crystalline nature of the as-synthesized VO₂(B).

2.2 Electrochemical performance of the VO₂(B) nanoflakes. The electrochemical performance of the VO₂(B) nanoflakes was evaluated in CR2032 coin-cells using a 1 M ZnSO₄ aqueous electrolyte and zinc metal counter electrode in a potential window of 0.2-1.0 V (vs. Zn²⁺/Zn). **Figure 2a** shows the first three discharge-charge profiles of the VO₂(B) positive electrode at a current density of 100 mA g⁻¹. A high capacity of 249 mA h g⁻¹ was achieved after the first discharge. The following charge capacity was 220 mA h g⁻¹, corresponding to an initial columbic efficiency of 88%. Afterwards, the columbic efficiency rapidly increased to 99% at the

fifth cycle. A predominant sloping voltage profile was observed in the 0.8–0.4 V voltage range, suggesting a solid-solution reaction process. The high columbic efficiency and the almost coincident charge-discharge profiles indicated highly reversible Zn^{2+} insertion/deinsertion in the $\text{VO}_2(\text{B})$ electrode. The high electrochemical reversibility was also confirmed by the overlapped cyclic voltammetry (CV) curves (**Figure 2b**). Three pairs of redox peaks were observed at 0.44/0.56 V, 0.50/0.64 V, and 0.55/0.70 V, indicating a multistep Zn^{2+} insertion/deinsertion process. In order to rule out the possibility of H^+ or H_3O^+ insertion in the $\text{VO}_2(\text{B})$ electrode, which could bring about additional CV peaks, a three-electrode cell was fabricated and tested using $\text{VO}_2(\text{B})$ as working electrode, graphite rod as counter electrode and Ag/AgCl as reference electrode, with a pH = 4.2 sulfuric acid solution as electrolyte (The pH value was the same as that of the 1 M ZnSO_4 aqueous solution). The discharge capacity of this three-electrode cell was very small (**Figure S1**), indicating that only Zn^{2+} in the ZnSO_4 electrolyte involved in the insertion/deinsertion processes.

The cycling performance of the $\text{VO}_2(\text{B})/\text{Zn}$ battery at a 100 mA g^{-1} current density is exhibited in **Figure 2c**. A high discharge capacity of 249 mA h g^{-1} and $\sim 100\%$ columbic efficiency was obtained after 100 cycles, resulting in capacity retention of 79%. The rate capability of the $\text{VO}_2(\text{B})$ electrode was evaluated by increasing the current density from 100 to 2000 mA g^{-1} procedurally (**Figure 2d**). The discharge capacities were 289, 216, 194, 178, and 156 mA h g^{-1} at 100, 200, 500, 1000, 2000 mA g^{-1} , respectively. High capacity retention of 54% was obtained when the current density was increased 20 times from 100 to 2000 mA g^{-1} , indicating fast Zn^{2+} insertion/deinsertion in the $\text{VO}_2(\text{B})$ lattice. It is worth emphasizing that the as-synthesized $\text{VO}_2(\text{B})$ sample was not specially modified by conductive carbon or nanoengineering, which indicated that the excellent electrochemical performance reported here was a result of intrinsic fast Zn^{2+} storage property of $\text{VO}_2(\text{B})$. The superior Zn^{2+} storage property was also evidenced by the discharge-charge profiles, which showed almost the same shape and small polarization at different current densities (**Figure S2**). The long cycle durability and stability of the $\text{VO}_2(\text{B})/\text{Zn}$ battery was measured at a current density of 2000 mA g^{-1} (**Figure 2e**). After an initial activation process, the discharge capacity gradually stabilized and reached 136 mA h

g^{-1} at the 100th cycle. Then, the capacity slowly decreased to 100 mA h g^{-1} at the 2000th cycle with a high capacity retention of 74% with respect to the 100th cycle. Compared with other reported V-based cathode materials (**Table S1**), although $\text{VO}_2(\text{B})$ does not show the best electrochemical performance, the large capacity, high rate capability, and prolonged cycling stability of the presented $\text{VO}_2(\text{B})/\text{Zn}$ battery suggested that $\text{VO}_2(\text{B})$ is a promising positive electrode material for ARZBs for large scale energy storage and high power applications. Further work is suggested to improve the electrochemical performance of $\text{VO}_2(\text{B})$ using nanocrystallization and compositing.

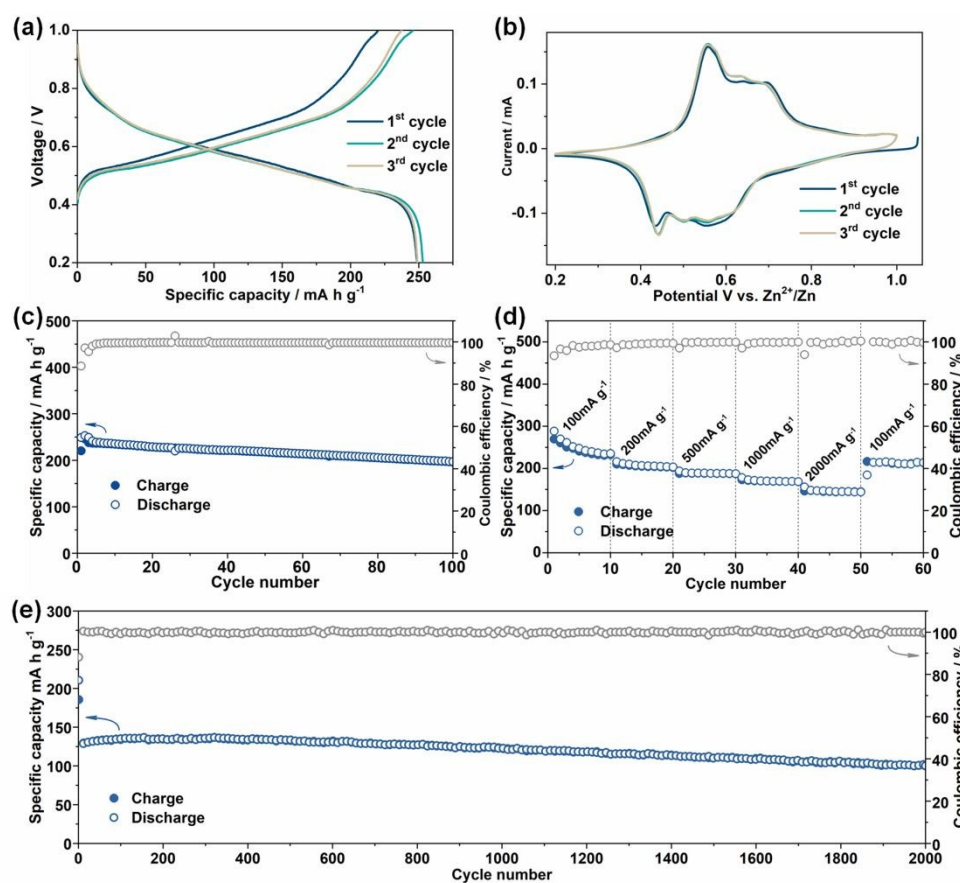


Figure 2. Electrochemical performances of $\text{VO}_2(\text{B})/\text{Zn}$ cells in 1 M ZnSO_4 electrolyte: (a) Discharge-charge profiles, (b) CV curves, (c) cycling performance at the current density of 100 mA g^{-1} , (d) rate capability, and (e) long cycling performance at the current density of 2000 mA g^{-1} .

2.3 Electrode reaction mechanisms. To gain deep insight into the phase evolutions of $\text{VO}_2(\text{B})$ during electrochemical reactions, *in operando* synchrotron diffraction was performed for the first discharge-charge cycle. **Figure 3a** shows the

contour maps of the *in operando* synchrotron diffraction patterns in selected 2 θ ranges. For the fresh cell, all the reflections could be indexed based on the monoclinic structure of VO₂(B) (Space group C2/m, see Rietveld refinement result in **Figure 3b**), which was in good agreement with the powder XRD result. No significant structural change was observed at the very beginning of the first discharge. Upon the discharge capacity reaching 10 mA h g⁻¹, corresponding to short discharge time of 13 min, a new reflection appeared at 1.08° (10.9 Å). In the meanwhile, some new reflections began to appear at 1.64° (7.2 Å), 2.16° (5.5 Å), 2.84° (4.2 Å), 3.66° (3.2 Å), 4.44° (2.7 Å), 4.63° (2.6 Å), 4.67° (2.5 Å), 4.79° (2.5 Å), 5.11° (2.3 Å), 5.18° (2.3 Å), 8.68° (1.4 Å), and 8.76° (1.4 Å) (**Figure S3**). These reflections could be indexed to a new (Zn(OH)₂)₃(ZnSO₄)·5H₂O phase (space group: *P*-1) with a large interplanar spacing of ~ 11 Å. This byproduct was also detected in some ARZBs using other vanadium oxides as positive electrodes³⁰. Note that these new reflections kept at the same positions during the whole discharge process, but their intensities kept growing. Especially, the intensity of the 1.08° reflection (10.9 Å) was extremely high at the end of discharge, suggesting preferential growth of the byproduct along the [001] direction.

Along with the growth of byproduct, the reflections of the VO₂(B) phase, such as those at 2.06° (5.8 Å), 3.37° (3.5 Å), 4.00° (3.0 Å), 4.46° (2.7 Å), 5.90° (2.0 Å), 6.41° (1.9 Å), 7.60° (1.6 Å), 8.15° (1.5 Å), and 8.72° (1.4 Å), slowly shifted to lower angles (larger lattice-plane distances), indicating a solid-solution process of the VO₂(B) phase. The Rietveld analysis showed that Zn_xVO₂ and (Zn(OH)₂)₃(ZnSO₄)·5H₂O coexisted at the end of discharge at 0.2 V (**Figure 3c**). It is worth noting that the solid-solution structure change of VO₂(B) in the aqueous ZnSO₄ electrolyte was quite different from that of VO₂(B) in organic LiPF₆ electrolyte which involved a two-phase transition with Li⁺ insertion³⁵. In the subsequent charge process, the reflections for (Zn(OH)₂)₃(ZnSO₄)·5H₂O gradually decreased and completely disappeared at the end of charge except the one at 1.08° (10.9 Å) which demonstrated the reversible formation/decomposition of the byproduct. Meanwhile, the reflections of the Zn²⁺-inserted VO₂(B) phase slowly returned back to their original positions, confirming the reversible structure change of VO₂(B) during Zn²⁺ insertion/deinsertion.

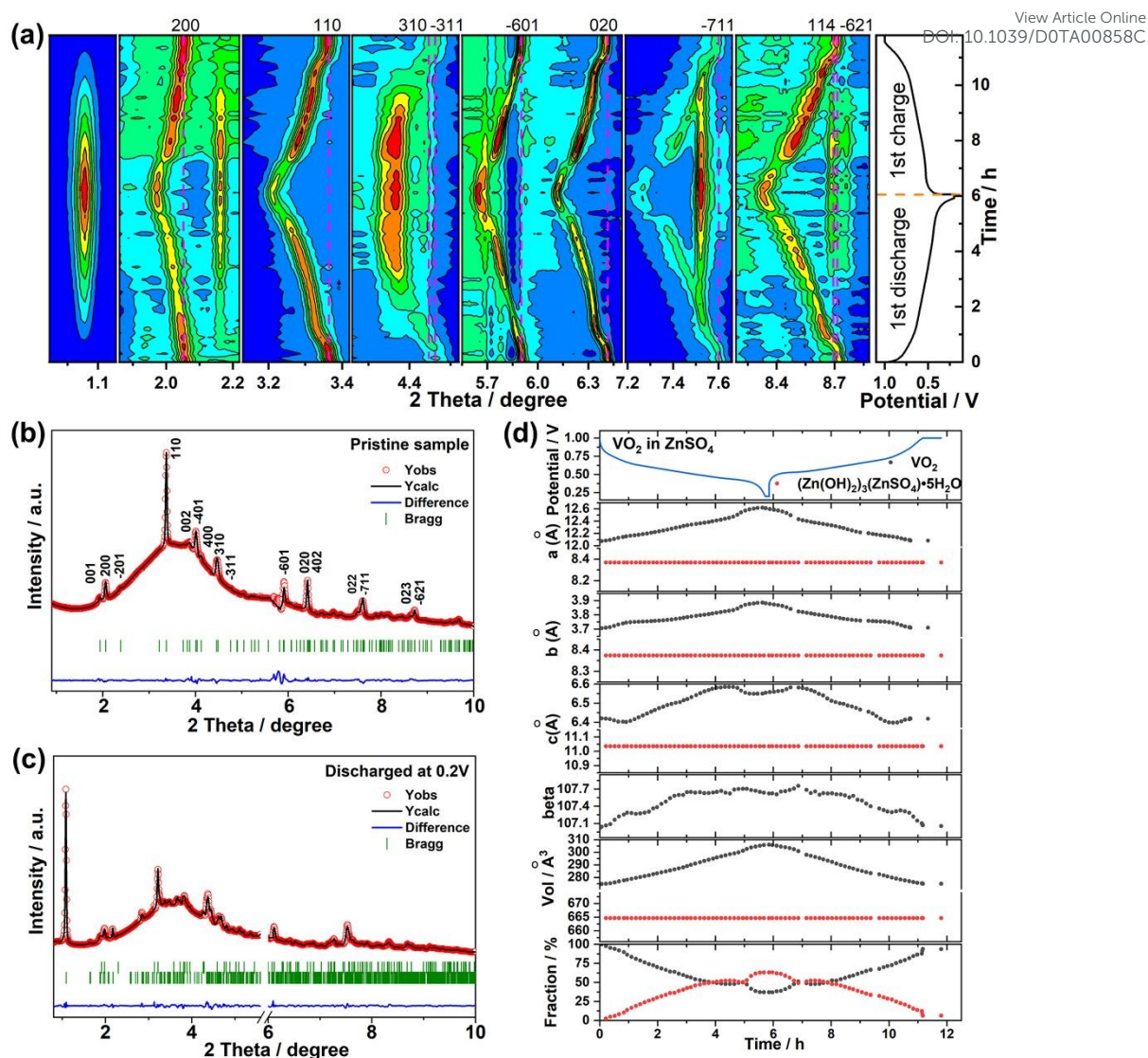


Figure 3. The phase evolutions of $\text{VO}_2(\text{B})$ during electrochemical reactions: (a) Contour maps of the *in operando* synchrotron diffraction patterns of $\text{VO}_2(\text{B})$ during the first discharge-charge and the corresponding voltage profiles at the current density of 50 mA g^{-1} ($\lambda=0.2072 \text{ \AA}$), Rietveld refinement from synchrotron diffraction data of (b) the pristine $\text{VO}_2(\text{B})$ and (c) the $\text{VO}_2(\text{B})$ electrode at the first discharged state of 0.2 V , and (d) Cell parameters and phase fraction of the $\text{VO}_2(\text{B})$ electrode during the first discharge-charge in 1 M ZnSO_4 electrolyte.

Detailed Rietveld refinement was performed to deeply reveal the reversible Zn^{2+} insertion/deinsertion into/from $\text{VO}_2(\text{B})$. Galvanostatic cycling showed $\sim 0.44 \text{ mol Zn}^{2+}$ inserted into $1.0 \text{ mol VO}_2(\text{B})$ during the first discharge. The structural parameters and phase ratios of Zn_xVO_2 and $(\text{Zn}(\text{OH})_2)_3(\text{ZnSO}_4)\cdot 5\text{H}_2\text{O}$ are shown in **Figure 3d**. During the whole discharge, Zn^{2+} inserted into the $\text{VO}_2(\text{B})$ electrode via a

solid-solution mechanism with significant increase of the a , b , c , and β lattice parameters. The a and b parameters of the final $\text{Zn}_{0.44}\text{VO}_2$ phase increased 4.54% and 4.86% with respect to those of the pristine $\text{VO}_2(\text{B})$, respectively, while the c and β parameters increased by 2.06% and 0.57%, respectively, resulting in an 11.47% volume expansion of the electrode. During the following charge process, the lattice parameters of the Zn_xVO_2 phase returned to their initial values, indicating reversibility of the structure change of the active material. Compared with other reported V-based cathode materials, in which two-phase transitions usually take place in ARZBs (**Table S1**), the structure of $\text{VO}_2(\text{B})$ was well maintained and the structure collapse was avoided due to the solid-solution mechanism, resulting in high reaction reversibility and prolonged cycle stability. The lattice parameters of $(\text{Zn}(\text{OH})_2)_3(\text{ZnSO}_4)\cdot 5\text{H}_2\text{O}$ remained unchanged during discharge (**Figure 3d**), but the relative amount of this byproduct kept increasing, which increased to 63 wt.% of the whole electrode at the end of discharge. Along with Zn^{2+} de-insertion, the relative amount of $(\text{Zn}(\text{OH})_2)_3(\text{ZnSO}_4)\cdot 5\text{H}_2\text{O}$ continuously decreased and almost totally disappeared at the end of charge, which confirmed the reversible decomposition of the byproduct.

In operando X-ray absorption spectroscopy (XAS) was carried out to probe the electronic structure and coordinative environment of V ions during electrochemical process. The edge positions of the V K-edge spectra measured at different voltages were compared with the reference spectra of V_2O_3 and VO_2 where V has +3 and +4 oxidation states, respectively. As shown in **Figure 4a**, the oxidation state of V was +4 in the initial state, which was in agreement with the +4 oxidation state of $\text{VO}_2(\text{B})$. An intense pre-edge peak on the X-ray absorption near edge structure (XANES) was observed for the pristine $\text{VO}_2(\text{B})$, which was attributed to transitions between the $1s$ and bound p -hybridized d -states, because of the distorted VO_6 octahedra in monoclinic $\text{VO}_2(\text{B})$ ⁴¹. The edge position of the V K-edge shifted to lower energies during the discharge process (**Figure 4a**). Meanwhile, the pre-edge peak (peak A in **Figure 4a**) also slightly shifted to lower energy close to the spectrum of V_2O_3 accompanying with the decrease of its intensity. The evidence identified the reduction of V ions and the changes in the local environment from a low degree of centro-symmetry to a higher degree of centro-symmetry during Zn^{2+} insertion. The

edge resonance (peak B in **Figure 4a**) showed big changes in both intensity and shape, which was related to energy absorption by core electrons^{41, 42}. During the discharge process, the shape of peak B changed from two broad peaks centered at ~ 5485.80 and 5489.60 eV to a single broad peak centered at 5486.10 eV and their intensity significantly increased. In the meanwhile, another peak centered at ~ 5504.60 eV strongly shifted to a lower energy at ~ 5496.80 eV along with a slight increase of intensity. Moreover, no distinct isosbestic point was observed during discharge, implying a solid-solution process along with Zn^{2+} insertion into $\text{VO}_2(\text{B})$ ^{42, 43}, which was fully in agreement with the above result proved by *in operando* synchrotron diffraction.

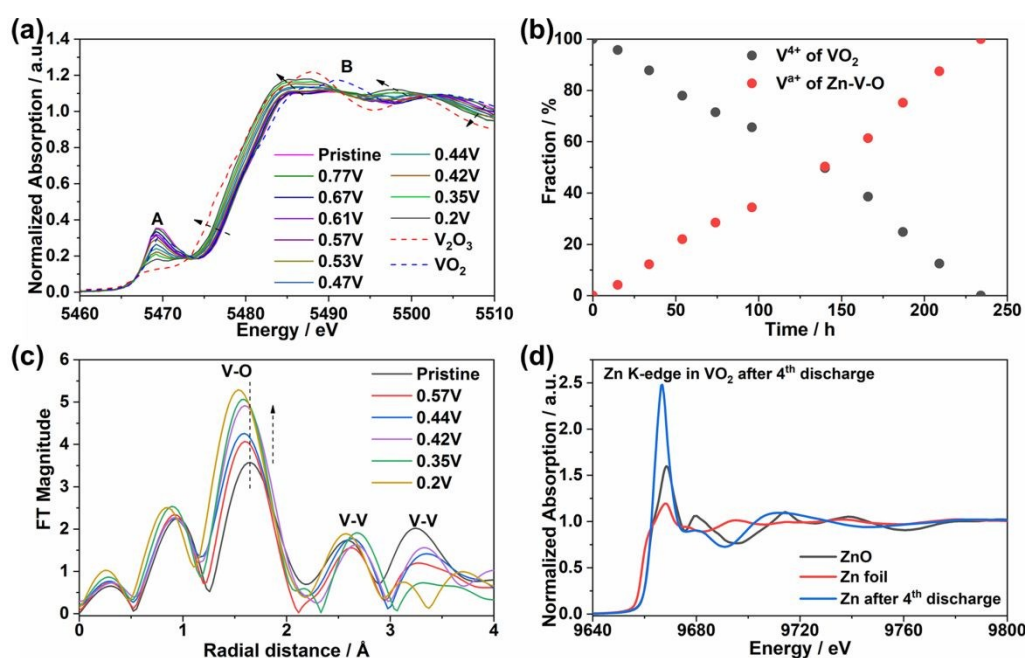


Figure 4. The electronic structure and coordinative environment changes of V and Zn ions during electrochemical process: (a) *in operando* V K-edge XANES spectra of the $\text{VO}_2(\text{B})$ electrode during the discharge process, (b) Relative change of the V valence during discharge process, (c) Fourier transforms (k^3 -weighted) of V K-edge EXAFS as a function of state of discharge, and (d) *ex situ* Zn K-edge XANES spectra of the $\text{VO}_2(\text{B})$ electrode.

In order to evaluate the V oxidation state at the end of discharge, a linear combination fitting (LCF) was performed using V_2O_3 and VO_2 as standards (**Figure S4**). Note that the fitting result was not good enough to get accurate valence states of Zn_xVO_2 , possibly due to the different symmetry and structures of the discharged

sample ($\text{Zn}_{0.395}\text{VO}_2$) and the chosen standards. Anyway, the V oxidation state of the discharged sample was approx. +3.26, which was very close to the value calculated from the electrochemical capacity (+3.21). The variations in the relative ratio of $\text{V}^{4+}/\text{V}^{3.26+}$ during discharge were also fitted using the XANES of the initial VO_2 and the discharged $\text{Zn}_{0.395}\text{VO}_2$ sample (**Figure 4b**). The relative amount of V^{4+} gradually decreased from 100% to 0 after 234 mins of discharge, while the relative amount of $\text{V}^{3.26+}$ gradually increased to 100% from 0, which was consistent with the reduction of V and resulted in the V oxidation state of +3.26 at the end of the first discharge. It should be noted that not all of the V cations were reduced to a lower oxidation state and a part of V^{4+} still existed in the electrode after the discharge process.

The phase uncorrected Fourier transform (FT) (k^3 -weighted) of selected V K-edge extended X-ray absorption fine structure (EXAFS) during the first discharge is shown in **Figure 4c**. Obviously, the amplitudes and phases of the EXAFS spectra varied in a significant way along with the increase of Zn^{2+} content in the $\text{VO}_2(\text{B})$ structure, indicating the local structure of V was strongly perturbed upon Zn^{2+} insertion. The pristine $\text{VO}_2(\text{B})$ displayed one FT peak around 1.7 Å, corresponding to the V-O bonds in VO_6 octahedra. The two FT peaks at around 2.6 Å and 3.2 Å were associated with the feature of V-V shells, which were in good agreement with our refinement result from synchrotron diffraction data and literature reports⁴⁴. The increased amplitude of V-O feature indicated a higher degree of symmetry for the local structure of V in the discharged state. Meanwhile, the shape and the overall position of the V-V feature changed as well, which proved the structure change of $\text{VO}_2(\text{B})$ during Zn^{2+} insertion.

Furthermore, *ex situ* Zn K-edge XAS was performed at the end of the 4th discharge using the same electrochemical test cell to study the oxidation state of Zn in the electrode. As shown in **Figure 4d**, the edge position of the Zn K-edge XANES overlapped with that of the ZnO standard, suggesting the +2 oxidation state of Zn ions. The FT peak at around 1.6 Å is typical of Zn-O bonds (k^3 -weighted, **Figure S5**). HRTEM analysis (**Figure S6**) further disclosed that the (110) interlayer spacing of the discharged $\text{Zn}_x\text{VO}_2(\text{B})$ was 0.37 nm, which was slightly larger than that of the pristine $\text{VO}_2(\text{B})$ (0.35 nm, Figure 1b) due to Zn^{2+} intercalation into $\text{VO}_2(\text{B})$. Another set of lattice stripes ($d = 1.11$ nm) was attributed to the $(\text{Zn}(\text{OH})_2)_3(\text{ZnSO}_4)\cdot 5\text{H}_2\text{O}$

byproduct, which covered the surface of VO₂(B) particles. The existence of Zn²⁺ was also confirmed by the clear Zn element signal in the elemental mapping for the VO₂(B) electrode at discharged state (**Figure S6**). Additionally, Raman analysis revealed that the characteristic Raman peaks of VO₂(B) were almost disappeared after discharge, except for two distinguished peaks at around 900 cm⁻¹ (**Figure S7**). This may be due to a great amount of byproduct grown on the surface of the electrode. As a result, the Raman signals of Zn_xVO₂(B) were masked by those of the byproduct. Theoretical calculations based on density functional theory (DFT) were conducted to further confirm the storage sites and diffusion pathways of Zn²⁺ in the VO₂(B) electrode. The lowest energy relaxed structures indicated that a VO₂(B) unit cell could accommodate four Zn²⁺ (Zn_{0.5}VO₂) with a volume change of 6.9% which was close to the *in operando* synchrotron diffraction results. The results showed that the Zn ions accommodated at two 2a Wyckoff sites, (0.93, 0, 0) and (0.15, 0, 0), both of which (green and yellow balls in **Figure S8**) are interstitial sites of VO₂(B). The inserted Zn²⁺ were surrounded by O atoms, which changed the local environment of the crystal. This was in accordance with the XANES data. Moreover, the diffusion kinetics of Zn²⁺ in VO₂(B) was studied by the climbing-image nudged elastic band method (CI-NEB method, see experimental in detail). There are two possible diffusion pathways for Zn²⁺ in the VO₂(B) framework, which are along the *b* and *c* axis, respectively, as shown in **Figure 5**. The result showed that the Zn²⁺ diffusion barriers along the *b* and *c* axis were 0.594 and 0.94 eV, respectively. According to Ceder *et al.* a reasonably small energy barrier of < 0.65 eV is required for diffusion of guest cations in an electrode material⁴⁵. Hence, the CI-NEB calculations suggested 1D diffusion of Zn²⁺ in the VO₂(B) crystal along the *b* axis.

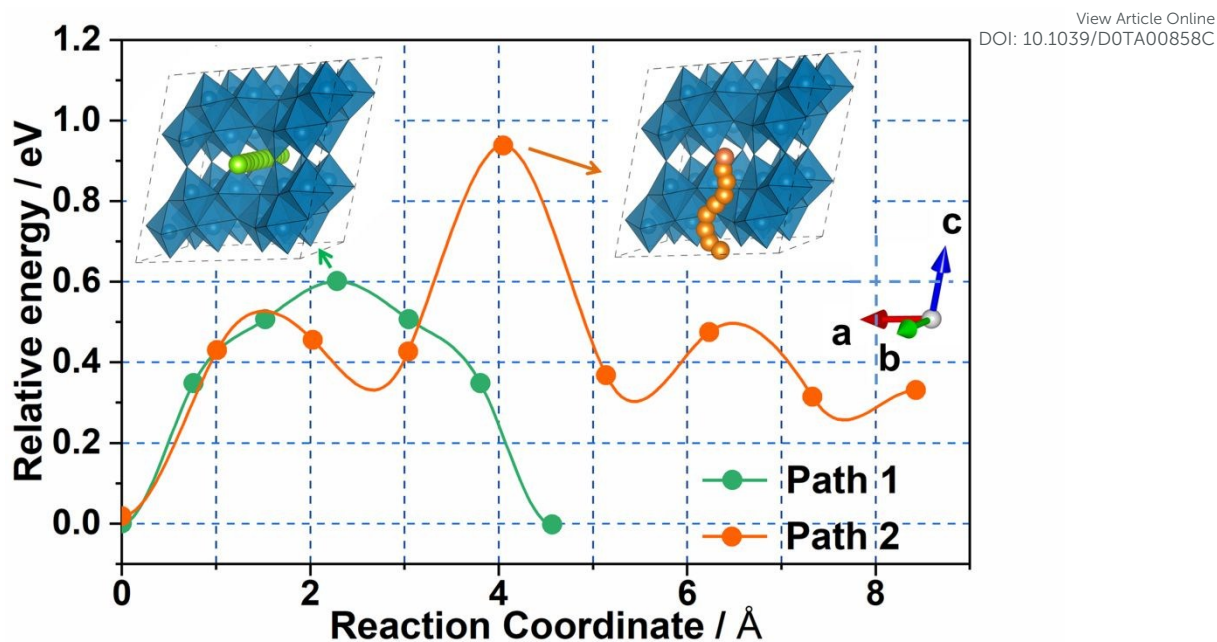


Figure 5. Zn^{2+} diffusion pathways in $\text{VO}_2(\text{B})$ and the corresponding diffusion energy barriers.

2.4 Influence of different electrolytes and byproducts. To reveal the influence of electrolytes and byproducts on the electrochemical properties of $\text{VO}_2(\text{B})/\text{Zn}$ aqueous batteries, the cycling performance and rate capability of the $\text{VO}_2(\text{B})/\text{Zn}$ electrochemical test cells using other two aqueous electrolytes, 1 M $\text{Zn}(\text{CF}_3\text{SO}_3)_2$ and 1 M $\text{Zn}(\text{NO}_3)_2$, were conducted and shown in **Figure 6a-b** and **6c-d**, respectively. The electrochemical performance of the cells using 1 M $\text{Zn}(\text{CF}_3\text{SO}_3)_2$ electrolyte was slightly better than that of the cells using 1 M ZnSO_4 electrolyte. Its remaining capacity after 100 cycles was 239 mA h g^{-1} , corresponding to a capacity retention of 81%. When the current density is increased to 2000 mA g^{-1} , the cell still exhibited a high capacity of 183 mA h g^{-1} . In spite of this, using $\text{Zn}(\text{CF}_3\text{SO}_3)_2$ in large scale energy storage devices seems unlikely due to economic concern, as the price of $\text{Zn}(\text{CF}_3\text{SO}_3)_2$ is 5-10 times higher than that of ZnSO_4 . By contrast, the performance of the cells using 1 M $\text{Zn}(\text{NO}_3)_2$ electrolyte was unsatisfying. The initial capacity was lower (186 mA h g^{-1}) and the discharge capacity underwent a dramatic decrease after a dozen cycles. Unsurprisingly, the capacity was negligible when the current densities increased to 1000 and 2000 mA g^{-1} . These results indicated that Zn^{2+} insertion into $\text{VO}_2(\text{B})$ was hindered in the 1 M $\text{Zn}(\text{NO}_3)_2$ aqueous electrolyte.

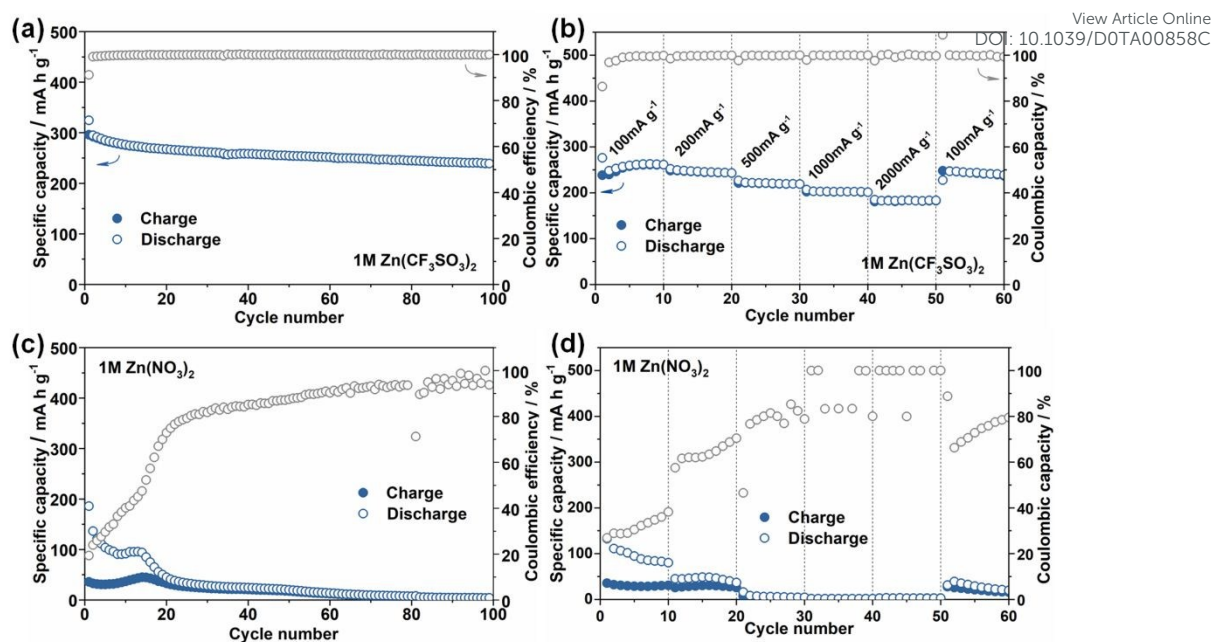


Figure 6. Electrochemical performances of VO₂(B)/Zn cells in different electrolytes: (a-b) Cycling performance (current density: 100 mA g⁻¹) and rate capability in 1 M Zn(CF₃SO₃)₂ electrolyte, respectively. (c-d) Cycling performance (current density: 100 mA g⁻¹) and rate capability in 1 M Zn(NO₃)₂ electrolyte, respectively.

The electrochemical performance of a battery system is related to many factors. Particularly, ionic diffusion in the electrode bulk and charge transfer process at the electrolyte/electrode interface are two of the most critical parameters. As shown in **Figure 7**, the Zn²⁺ diffusion coefficients (D_{Zn}) of the VO₂(B) electrodes using different aqueous electrolytes were calculated by employing the galvanostatic intermittent titration technique (GITT). The calculated D_{Zn} values were very similar to each other, about 10⁻⁹ to 10⁻¹⁰ cm² s⁻¹, which were comparable with the Li⁺ diffusion coefficients of LiFePO₄⁴⁶ and LiCoO₂⁴⁷ in electrochemical test cells with organic electrolytes. This result revealed that, on one hand, VO₂(B) as a positive electrode could allow fast Zn²⁺ diffusion, giving rise to good rate capability. On the other hand, the large differences in electrochemical performance of VO₂(B) with different electrolytes did not arise from bulk Zn²⁺ diffusion.

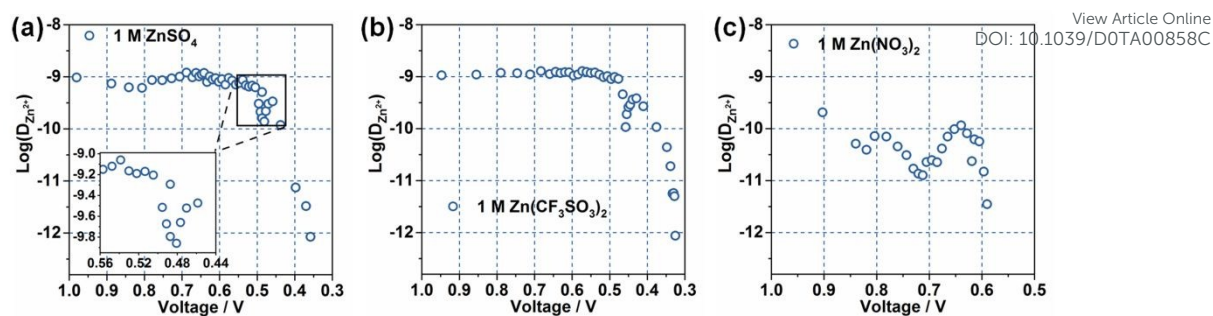


Figure 7. Zn^{2+} diffusion coefficients of the $\text{VO}_2(\text{B})$ electrode in different aqueous electrolytes: (a) 1 M ZnSO_4 , (b) 1 M $\text{Zn}(\text{CF}_3\text{SO}_3)_2$, and (c) 1 M $\text{Zn}(\text{NO}_3)_2$.

Hence, electrochemical impedance spectroscopy (EIS) which is sensitive to charge transfer processes at the electrolyte/electrode interface, was employed to further study the reasons of the different electrochemical performances of $\text{VO}_2(\text{B})$ in different aqueous electrolytes. All the cells were discharged to different voltages and rested for 2 h to reach a quasi-equilibrium state before the EIS measurements. As shown in **Figure S9**, all the Nyquist plots consisted of one semicircle and a slope line. According to literature⁴⁸, the intercept of Z' axis at high frequency was corresponding to solution and contact resistance (R_s). The semicircle in the high to medium frequency region was attributed to the byproduct formation and charge transfer process at the electrolyte/electrode interface, which was assigned as R_{total} in the present work due to the difficulty in separating these two components during data fitting. The slope line in the low-frequency region was attributed to Zn^{2+} diffusion in the electrode bulk (Z_w). At OCV and 0.8 V, the R_{total} in 1 M ZnSO_4 was the smallest compared with other systems. Along with further discharging to 0.2 V, the R_{total} values in 1 M $\text{Zn}(\text{CF}_3\text{SO}_3)_2$ were always the smallest among the three electrolyte systems. This result was in agreement with the superior rate capability and cycling stability in the 1 M $\text{Zn}(\text{CF}_3\text{SO}_3)_2$ electrolyte. The cell using 1 M $\text{Zn}(\text{NO}_3)_2$ electrolyte showed always the largest R_{total} , resulting in the worst electrochemical performance. The above results demonstrated that the electrochemical performance of the $\text{VO}_2(\text{B})/\text{Zn}$ cells were largely dependent on the charge transfer process between the liquid electrolyte and the solid electrode as well as its interface byproduct resistance.

A typical charge transfer process involved multiple steps including desolvation/resolvation of ionic charge carriers with their solvation shell, and sorption/desorption of ions and electrons. In aqueous solutions, Zn^{2+} are typically

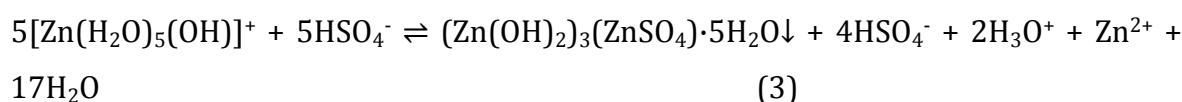
six-coordinated with water molecules, existing as a $[\text{Zn}(\text{H}_2\text{O})_6]^{2+}$ complex⁴⁹. The key processes involved in the $\text{VO}_2(\text{B})/\text{Zn}$ cell with ZnSO_4 electrolyte during discharge and charge is shown in **Scheme 1**. The water molecules in the $[\text{Zn}(\text{H}_2\text{O})_6]^{2+}$ complex are strongly polarized by the high charge density of the central divalent cation, which leads to spontaneous hydrolysis as given in reaction (1)⁵⁰ using ZnSO_4 electrolyte as an example:



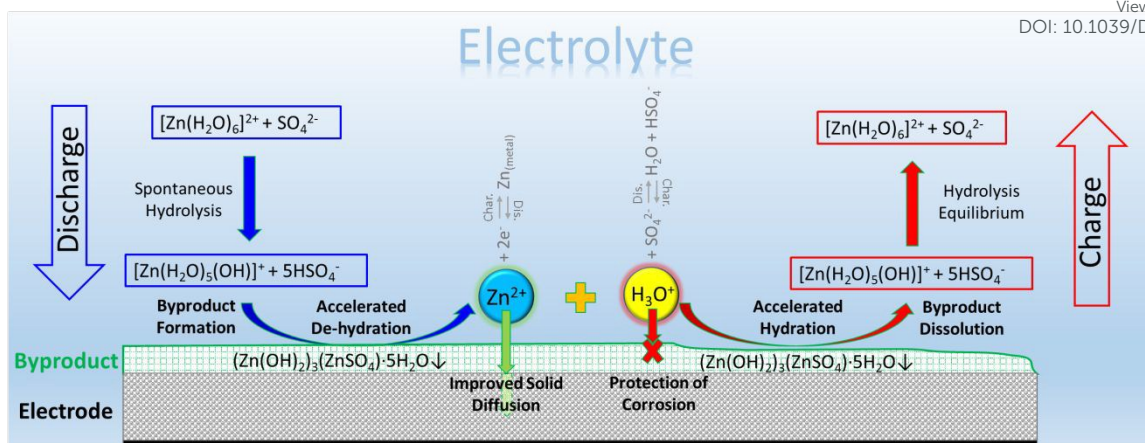
The high ionic charge of the central Zn^{2+} cation is screened by the coordinating OH^- anionic species and redistributed by the partial charges formed by polarized intimate water molecules. Obviously, it is impossible that such big and complex $[\text{Zn}(\text{H}_2\text{O})_5(\text{OH})]^+$ ions could freely insert/deinsert in the $\text{VO}_2(\text{B})$ lattice. Therefore, a desolvation process must occur at the electrolyte/electrode interface before Zn^{2+} insert into $\text{VO}_2(\text{B})$. On the other hand, according to the acidity constant of HSO_4^- , $K_a = 10^{-2} = [\text{H}_3\text{O}^+][\text{SO}_4^{2-}]/[\text{HSO}_4^-]$ ⁵¹, the $[\text{HSO}_4^-]$ was about $10^{-2.2}$ mol/L for the initial electrolyte, which was around 100 times higher than the H_3O^+ concentration in the electrolyte (pH=4.2, $10^{-4.2}$ mol/L).



Hence, an equilibrium equation is proposed as below:



In this case, the formation of $(\text{Zn}(\text{OH})_2)_3(\text{ZnSO}_4) \cdot 5\text{H}_2\text{O}$ byproduct could accelerate the desolvation of $[\text{Zn}(\text{H}_2\text{O})_6]^{2+}$ into Zn^{2+} during the discharge process and therefore facilitated insertion of Zn^{2+} into the $\text{VO}_2(\text{B})$ electrode. During the charge process, Zn^{2+} was extracted from the $\text{VO}_2(\text{B})$ structure, resulting in the left shift of the above equilibrium equation (3). Hence, the byproduct was disappearing on the positive electrode side.



Scheme 1. Schematic diagram of the key processes involved in $\text{VO}_2(\text{B})/\text{Zn}$ cell with ZnSO_4 electrolyte during the discharge and charge processes.

The number of Zn^{2+} inserted into 1 mol $\text{VO}_2(\text{B})$ was ~ 0.44 mol according to the practical capacity of the first discharge. Accordingly, if all the Zn^{2+} desolvated through equation (3) were inserted into $\text{VO}_2(\text{B})$, the amount of $(\text{Zn}(\text{OH})_2)_3(\text{ZnSO}_4)\cdot 5\text{H}_2\text{O}$ byproduct should be 0.44 mol at the end of discharge, resulting in a weight ratio of $(\text{Zn}(\text{OH})_2)_3(\text{ZnSO}_4)\cdot 5\text{H}_2\text{O}/\text{Zn}_{0.44}\text{VO}_2$ as 2.16. However, this ratio was slightly larger than the value of 1.7 obtained from the *in operando* XRD refinement result, which may give a hint that part of the $(\text{Zn}(\text{OH})_2)_3(\text{ZnSO}_4)\cdot 5\text{H}_2\text{O}$ byproduct reacted with the formed H_3O^+ . On the other hand, the produced H_3O^+ during the desolvation of $[\text{Zn}(\text{H}_2\text{O})_6]^{2+}$ could also be partly consumed through the equilibrium equation (2) shifted to left side, thus keeping the relatively stable pH value of the electrolyte and protecting the electrode material. This was in accordance with the recently reported result that the pH value of the electrolyte slightly increased after discharge⁵². This also suggested that the byproduct formation was mainly related to the desolvation process. So it is reasonable that the byproduct would be produced during Zn plating. Moreover, the Zn stripping would increase the concentration of Zn^{2+} , resulting in the direct formation of $[\text{Zn}(\text{H}_2\text{O})_6]^{2+}$ because of the massive presence of H_2O molecules. This might cause the right shift of the equilibrium equations (1) and (3) and therefore, led to the formation of byproduct. To confirm this, we carried out a comparison experiment to study the byproduct formation in different electrolytes. A coin cell was assembled with Ti foil and Zn foil in three different electrolytes. XRD measurements were carried out to confirm the phases of the byproducts (**Figure S10**). Except for some characteristic reflections from the Ti foil, a

(Zn(OH)₂)₃(ZnSO₄)·5H₂O phase with an interlayer distance about 11 Å was confirmed for the byproduct formed in the 1 M ZnSO₄ electrolyte, which was in agreement with the *in operando* synchrotron diffraction results. Other two byproducts with interlayer distances of ~10 Å and ~13 Å were discovered on the electrodes plated in Zn(NO₃)₂ and Zn(CF₃SO₃)₂ electrolytes, respectively. The byproduct formed in Zn(NO₃)₂ electrolyte was (Zn(OH)₂)₄(Zn(NO₃)₂)·2H₂O, and that produced in Zn(CF₃SO₃)₂ electrolyte could be ascribed to Zn_x(CF₃SO₃)_y(OH)_{2x-y}·nH₂O as observed in recent work⁵³⁻⁵⁵. For example, Zn_x(CF₃SO₃)_y(OH)_{2x-y}·nH₂O byproduct was observed from *in operando* XRD study of α-MnO₂ and V₃O₇·H₂O cathode material in Zn(CF₃SO₃)₂ electrolyte⁵³. Additionally, Zn_x(CF₃SO₃)_y(OH)_{2x-y}·nH₂O was also synthesized by adding KOH solution into Zn(CF₃SO₃)₂ electrolyte and proved by *ex situ* XRD^{55, 56}. The byproduct was irreversibly formed/disappeared with increased/decreased pH of the Zn(CF₃SO₃)₂ aqueous electrolyte⁵⁶, which is similar to the reported Zn₄SO₄(OH)₆·xH₂O formation/decomposition along with the increase/decrease of pH in ZnSO₄ electrolyte⁵² in aqueous Zn||ZnSO₄||MnO₂ batteries. Despite the different byproducts formed in different electrolytes, *ex-situ* XRD (**Figure S11**) demonstrated that the positions of the characteristic peaks of Zn_xVO₂(B) were almost the same for different electrolytes. This indicates that the energy storage mechanism of VO₂(B) in different aqueous electrolytes was similar except the formation of byproduct. After Zn plating on Ti foil (Zn stripping on Zn negative electrode), the byproducts on the Zn negative electrode in the 1 M ZnSO₄ electrolyte was also observed by XRD (**Figure S12**), which confirmed our hypothesis on the byproduct formation during Zn stripping. These results demonstrated that the formation of byproducts in ARZBs is a very common phenomenon. In addition, the structure and morphology of the byproducts varied with the applied electrolytes (**Figure S13**). Note that the ARZBs in which the byproduct had the largest interlayer distance showed the best electrochemical performance.

To further understand the influence of byproducts on ARZBs' electrochemistry, bond valence sum maps (BVSM) were calculated in the BondSTR program of the FullProf Suite using the soft bond valence sum parameters developed by S. Adams^{57, 58}. Therefore, the possible diffusion pathways can be determined by increasing ΔV to the minimal values necessary to connect the mobile cation sites into a continuous

network. Although the BVSM method does not include repulsions from neighboring cations, this method has been successfully applied to estimate the diffusion pathways in battery materials^{59,60}. As shown in **Figure S14**, a surface level corresponding to the value of 1.2 eV above the minimum was chosen to plot the bond valence energy landscapes (BVEL). This corresponded to an infinitely connected surface for Zn²⁺ transport. It revealed that Zn²⁺ transport can occur through a three-dimensional pathway. By comparing the BVEL of (Zn(OH)₂)₃(ZnSO₄)·5H₂O and (Zn(OH)₂)₄(Zn(NO₃)₂)·2H₂O with the same iso-surface value of 1.2 eV over the minimum energy, one can see less iso-surface density for (Zn(OH)₂)₄(Zn(NO₃)₂)·2H₂O, probably suggesting the worse Zn²⁺ diffusion ability in its pathways compared with that of (Zn(OH)₂)₃(ZnSO₄)·5H₂O. These results demonstrated that, on one hand, the desolvation of Zn²⁺ can be activated along with the formation of byproducts. On the other hand, the formed byproduct could facilitate the migration of Zn²⁺ on the surface of the electrodes due to the three-dimensional pathways of the byproducts because of their large interlayer distances.

3. Conclusions

ARZBs are becoming a very promising battery technology for large scale energy storage thanks to their high safety, low cost, and abundance of material resources. However, the commercial applications of ARZBs are still hindered by the restricted rate capability and cycle life of the positive electrode materials. In this work, monoclinic VO₂(B) nanoflakes were prepared by a hydrothermal method, which exhibited superior Zn²⁺ storage performances in the 1 M ZnSO₄ aqueous electrolyte including large specific capacity, high rate capability, and good cycling stability. *In operando* synchrotron X-ray diffraction demonstrated that the material underwent a highly reversible solid-solution reaction between VO₂(B) and Zn_{0.44}VO₂ together with the reversible formation/decomposition of a (Zn(OH)₂)₃(ZnSO₄)·5H₂O byproduct. *In operando* X-ray absorption spectroscopy revealed the reduction of V ions during Zn²⁺ insertion. In particular, the formation of byproduct was attributed to the dehydration of [Zn(H₂O)₆]²⁺, where the byproduct also played a very important role in protecting the electrodes from side reactions with H₃O⁺. However, different byproducts could be formed on the electrode depending on the aqueous electrolytes used in ARZBs. As a result, the electrochemical performance of ARZBs was largely determined by the

structure and composition of the byproducts. BVSM analysis showed that the byproducts could facilitate the migration of Zn^{2+} on the electrode surface due to the three-dimensional pathways of the byproducts. Therefore, a byproduct with largely expanded migration pathways could facilitate the charge transfer of Zn^{2+} on the electrode surface. In this regard, the 1 M $\text{Zn}(\text{CF}_3\text{SO}_3)_2$ electrolyte was proven a more appropriate electrolyte for $\text{VO}_2(\text{B})$ due to the largest interlayer spacing ($\sim 13 \text{ \AA}$) of its byproduct among all electrolytes investigated in this work. This comprehensive study may help researchers to understand the Zn^{2+} storage process in $\text{VO}_2(\text{B})$ and the importance of interfacial reactions between the electrolyte and electrode in ARZBs.

Conflicts of interest

There are no conflicts to declare.

Supporting Information

Supporting Information, including Experimental, Table S1, and Figure S1-S14, is available.

Acknowledgements

This work was supported by the National Natural Science Foundation of China (No. 21773091, 51972140) and Department of Science and Technology of Jilin Province (No. 20180414004GH) and China Postdoctoral Science Foundation funded project (No. 2019M651198). This work contributed to the research performed at CELEST (Center for Electrochemical Energy Storage Ulm-Karlsruhe) and was partially funded by the German Research Foundation (DFG) under Project ID 390874152 (POLiS Cluster of Excellence). Our work was also gained benefit from the beamtime allocation at PETRA-III beamlines P02.1 and P65 at DESY, Hamburg, Germany. We express our thanks to Dr. Martin Etter and Dr. Edmund Welter from DESY. The *in operando* XAS work was performed by using the Biologic potentiostat of PETRA-III beamline P02.1. We thank Dr. Michael Knapp for his fruitful discussion about structure investigation from the synchrotron diffraction data.

Reference:

1. G. Fang, J. Zhou, A. Pan and S. Liang, *ACS Energy Letters*, 2018, **3**, 2480-2501.
2. M. Song, H. Tan, D. Chao and H. J. Fan, *Advanced Functional Materials*, 2018, **28**, 1802564.
3. P. Yu, Y. X. Zeng, H. Z. Zhang, M. H. Yu, Y. X. Tong and X. Lu, *Small*, 2019, **15**, 1804760.
4. B. Lee, H. R. Lee, H. Kim, K. Y. Chung, B. W. Cho and S. H. Oh, *Chemical communications*, 2015, **51**, 9265-9268.
5. A. Konarov, N. Voronina, J. H. Jo, Z. Bakenov, Y. K. Sun and S. T. Myung, *ACS Energy Letters*, 2018, **3**, 2620-2640.
6. L. Zhang, L. Chen, X. Zhou and Z. Liu, *Scientific reports*, 2015, **5**, 18263.
7. L. Zhang, L. Chen, X. Zhou and Z. Liu, *Advanced Energy Materials*, 2015, **5**, 1400930.
8. R. Trócoli and F. La Mantia, *ChemSusChem*, 2015, **8**, 481-485.
9. C. Xu, B. Li, H. Du and F. Kang, *Angewandte Chemie*, 2012, **51**, 933-935.
10. H. Pan, Y. Shao, P. Yan, Y. Cheng, K. S. Han, Z. Nie, C. Wang, J. Yang, X. Li, P. Bhattacharya, K. T. Mueller and J. Liu, *Nature Energy*, 2016, **1**, 16039.
11. S. Islam, M. H. Alfaruqi, V. Mathew, J. Song, S. Kim, S. Kim, J. Jo, J. P. Baboo, D. T. Pham, D. Y. Putro, Y. K. Sun and J. Kim, *Journal of Materials Chemistry A*, 2017, **5**, 23299-23309.
12. A. Baby, B. Senthilkumar and P. Barpanda, *ACS Applied Energy Materials*, 2019, **2**, 3211-3219.
13. N. Zhang, F. Cheng, Y. Liu, Q. Zhao, K. Lei, C. Chen, X. Liu and J. Chen, *Journal of the American Chemical Society*, 2016, **138**, 12894-12901.
14. M. H. Alfaruqi, V. Mathew, J. Gim, S. Kim, J. Song, J. P. Baboo, S. H. Choi and J. Kim, *Chemistry of Materials*, 2015, **27**, 3609-3620.
15. M. H. Alfaruqi, J. Gim, S. Kim, J. Song, D. T. Pham, J. Jo, Z. Xiu, V. Mathew and J. Kim, *Electrochemistry Communications*, 2015, **60**, 121-125.
16. M. Sun, D.-S. Li, Y.-F. Wang, W.-L. Liu, M.-M. Ren, F.-G. Kong, S.-J. Wang, Y.-Z. Guo and Y.-M. Liu, *ChemElectroChem*, 2019, **6**, 2510-2516.
17. B. Jiang, C. Xu, C. Wu, L. Dong, J. Li and F. Kang, *Electrochimica Acta*, 2017, **229**, 422-428.
18. N. Zhang, Y. Dong, M. Jia, X. Bian, Y. Wang, M. Qiu, J. Xu, Y. Liu, L. Jiao and F. Cheng, *ACS Energy Letters*, 2018, **3**, 1366-1372.
19. J. Zhou, L. Shan, Z. Wu, X. Guo, G. Fang and S. Liang, *Chemical communications*, 2018, **54**, 4457-4460.
20. X. Chen, L. Wang, H. Li, F. Cheng and J. Chen, *Journal of Energy Chemistry*, 2019, **38**, 20-25.
21. D. Kundu, B. D. Adams, V. Duffort, S. H. Vajargah and L. F. Nazar, *Nature Energy*, 2016, **1**, 16119.
22. X. Chuan, G. Jing, L. Peng, Z. Xixiang and A. H. N., *Angewandte Chemie International Edition*, 2018, **57**, 3943-3948.
23. X. Guo, G. Fang, W. Zhang, J. Zhou, L. Shan, L. Wang, C. Wang, T. Lin, Y. Tang and S. Liang, *Advanced Energy Materials*, 2018, **8**, 1801819.
24. P. He, G. Zhang, X. Liao, M. Yan, X. Xu, Q. An, J. Liu and L. Mai, *Advanced Energy Materials*, 2018, **8**, 1702463.

View Article Online
DOI: 10.1039/D0TA00858C

25. Y. Mengyu, H. Pan, C. Ying, W. Shanyu, W. Qiulong, Z. Kangning, X. Xu, A. Qinyou, S. Yi, S. Yuyan, M. K. T., M. Liqiang, L. Jun and Y. Jihui, *Advanced Materials*, 2018, **30**, 1703725. View Article Online
DOI: 10.1039/C8TA00858C
26. M. H. Alfaruqi, V. Mathew, J. Song, S. Kim, S. Islam, D. T. Pham, J. Jo, S. Kim, J. P. Baboo, Z. Xiu, K.-S. Lee, Y.-K. Sun and J. Kim, *Chemistry of Materials*, 2017, **29**, 1684-1694.
27. J. H. Jo, Y.-K. Sun and S.-T. Myung, *Journal of Materials Chemistry A*, 2017, **5**, 8367-8375.
28. J. Ming, J. Guo, C. Xia, W. Wang and H. N. Alshareef, *Materials Science and Engineering: R: Reports*, 2019, **135**, 58-84.
29. B. Sambandam, V. Soundharrajan, S. Kim, M. H. Alfaruqi, J. Jo, S. Kim, V. Mathew, Y. K. Sun and J. Kim, *Journal of Materials Chemistry A*, 2018, **6**, 3850-3856.
30. V. Soundharrajan, B. Sambandam, S. Kim, M. H. Alfaruqi, D. Y. Putro, J. Jo, S. Kim, V. Mathew, Y. K. Sun and J. Kim, *Nano Letters*, 2018, **18**, 2402-2410.
31. F. Wan, L. Zhang, X. Dai, X. Wang, Z. Niu and J. Chen, *Nature communications*, 2018, **9**, 1656.
32. B. Y. Tang, J. Zhou, G. Z. Fang, F. Liu, C. Y. Zhu, C. Wang, A. Q. Pan and S. Q. Liang, *Journal of Materials Chemistry A*, 2019, **7**, 940-945.
33. M. Liu, B. Su, Y. Tang, X. Jiang and A. Yu, *Advanced Energy Materials*, 2017, **7**, 1700885.
34. X. Dai, F. Wan, L. Zhang, H. Cao and Z. Niu, *Energy Storage Materials*, 2018, **17**, 143-150.
35. Q. Liu, G. Tan, P. Wang, S. C. Abeyweera, D. Zhang, Y. Rong, Y. A. Wu, J. Lu, C.-J. Sun, Y. Ren, Y. Liu, R. T. Muehleisen, L. B. Guzowski, J. Li, X. Xiao and Y. Sun, *Nano Energy*, 2017, **36**, 197-205.
36. J. Ding, Z. Du, L. Gu, B. Li, L. Wang, S. Wang, Y. Gong and S. Yang, *Advanced Materials*, 2018, **30**, 1800762.
37. J. S. Park, J. H. Jo, Y. Aniskevich, A. Bakavets, G. Ragoisha, E. Streltsov, J. Kim and S. T. Myung, *Chemistry of Materials*, 2018, **30**, 6777-6787.
38. T. Wei, Q. Li, G. Yang and C. Wang, *Journal of Materials Chemistry A*, 2018, **6**, 8006-8012.
39. L. Chen, Y. Ruan, G. Zhang, Q. Wei, Y. Jiang, T. Xiong, P. He, W. Yang, M. Yan, Q. An and L. Mai, *Chemistry of Materials*, 2019, **31**, 699-706.
40. Z. Li, S. Ganapathy, Y. Xu, Z. Zhou, M. Sarilar and M. Wagemaker, *Advanced Energy Materials*, 2019, **9**, 1900237.
41. J. Wong, F. W. Lytle, R. P. Messmer and D. H. Maylotte, *Physical Review B*, 1984, **30**, 5596-5610.
42. Q. Fu, A. Sarapulova, V. Trouillet, L. Zhu, F. Fauth, S. Mangold, E. Welter, S. Indris, M. Knapp, S. Dsoke, N. Bramnik and H. Ehrenberg, *Journal of the American Chemical Society*, 2019, **141**, 2305-2315.
43. X. Liu, D. Wang, G. Liu, V. Srinivasan, Z. Liu, Z. Hussain and W. Yang, *Nature communications*, 2013, **4**, 2568.
44. Y. Oka, T. Yao, N. Yamamoto, Y. Ueda and A. Hayashi, *Journal of Solid State Chemistry*, 1993, **105**, 271-278.
45. Z. Q. Rong, R. Malik, P. Canepa, G. S. Gautam, M. Liu, A. Jain, K. Persson and G. Ceder, *Chemistry of Materials*, 2015, **27**, 6016-6021.

46. A. V. Churikov, A. V. Ivanishchev, I. A. Ivanishcheva, V. O. Sycheva, N. R. Khasanova and E. V. Antipov, *Electrochimica Acta*, 2010, **55**, 2939-2950. View Article Online
DOI: 10.1039/D0TA00858C
47. H. Yan, X. Huang, H. Li and L. Chen, *Solid State Ionics*, 1998, **113-115**, 11-15.
48. T. Hang, D. Mukoyama, H. Nara, N. Takami, T. Momma and T. Osaka, *Journal of Power Sources*, 2013, **222**, 442-447.
49. B. J. Mhin, S. Lee, S. J. Cho, K. Lee and K. S. Kim, *Chemical Physics Letters*, 1992, **197**, 77-80.
50. W. Wang and D. B. Breisinger, *Metallurgical and Materials Transactions B*, 1998, **29**, 1157-1166.
51. H. Sippola and P. Taskinen, *Journal of Chemical & Engineering Data*, 2014, **59**, 2389-2407.
52. B. Lee, H. R. Seo, H. R. Lee, C. S. Yoon, J. H. Kim, K. Y. Chung, B. W. Cho and S. H. Oh, *ChemSusChem*, 2016, **9**, 2948-2956.
53. P. Oberholzer, E. Tervoort, A. Bouzid, A. Pasquarello and D. Kundu, *ACS applied materials & interfaces*, 2018, DOI: 10.1021/acsami.8b16284.
54. L. Wang, K.-W. Huang, J. Chen and J. Zheng, *Science Advances*, 2019, **5**, eaax4279.
55. Q. Li, Y. Liu, K. Ma, G. Yang and C. Wang, *Small Methods*, 2019, **3**, 1900637.
56. L. Dong, W. Yang, W. Yang, C. Wang, Y. Li, C. Xu, S. Wan, F. He, F. Kang and G. Wang, *Nano-Micro Letters*, 2019, **11**, 94.
57. S. Adams and J. Swenson, *Physical Review B*, 2000, **63**, 054201.
58. S. Adams, in *Bond Valences*, eds. I. D. Brown and K. R. Poeppelmeier, Springer Berlin Heidelberg, Berlin, Heidelberg, 2014, DOI: 10.1007/430_2013_96, pp. 91-128.
59. M. Sun, G. Rousse, A. M. Abakumov, M. Saubanère, M.-L. Doublet, J. Rodríguez-Carvajal, G. Van Tendeloo and J.-M. Tarascon, *Chemistry of Materials*, 2015, **27**, 3077-3087.
60. B. Wen, J. Liu, N. A. Chernova, X. Wang, Y. Janssen, F. Omenya, P. G. Khalifah and M. S. Whittingham, *Chemistry of Materials*, 2016, **28**, 2229-2235.

Table of contents entry

Byproduct protects the vanadium-based positive electrode of ARZBs and facilitates Zn^{2+} insertion in the electrode.

